



A comparison of smartphone and infrasound microphone data from a fuel air explosive and a high explosive

September 2024

Changing the World's Energy Future

Samuel Kei Takazawa, Sarah Popenhagen, Milton Garces, Luis A Ocampo Giraldo, Edna S Cardenas, Jay D Hix, Scott J Thompson, David L Chichester



DISCLAIMER

This information was prepared as an account of work sponsored by an agency of the U.S. Government. Neither the U.S. Government nor any agency thereof, nor any of their employees, makes any warranty, expressed or implied, or assumes any legal liability or responsibility for the accuracy, completeness, or usefulness, of any information, apparatus, product, or process disclosed, or represents that its use would not infringe privately owned rights. References herein to any specific commercial product, process, or service by trade name, trade mark, manufacturer, or otherwise, does not necessarily constitute or imply its endorsement, recommendation, or favoring by the U.S. Government or any agency thereof. The views and opinions of authors expressed herein do not necessarily state or reflect those of the U.S. Government or any agency thereof.

A comparison of smartphone and infrasound microphone data from a fuel air explosive and a high explosive

**Samuel Kei Takazawa, Sarah Popenhagen, Milton Garces, Luis A Ocampo
Giraldo, Edna S Cardenas, Jay D Hix, Scott J Thompson, David L Chichester**

September 2024

**Idaho National Laboratory
Idaho Falls, Idaho 83415**

<http://www.inl.gov>

**Prepared for the
U.S. Department of Energy
Under DOE Idaho Operations Office
Contract DE-AC07-05ID14517**

SEPTEMBER 04 2024

A comparison of smartphone and infrasound microphone data from a fuel air explosive and a high explosive

S. K. Takazawa ; S. K. Popenhagen ; L. A. Ocampo Giraldo ; E. S. Cardenas ; J. D. Hix ; S. J. Thompson; D. L. Chichester ; M. A. Garcés 



J. Acoust. Soc. Am. 156, 1509–1523 (2024)

<https://doi.org/10.1121/10.0028379>



View
Online










Export
Citation



LEARN MORE

Advance your science and career as a member of the
Acoustical Society of America

A comparison of smartphone and infrasound microphone data from a fuel air explosive and a high explosive

S. K. Takazawa,^{1,a)}  S. K. Popenhagen,¹  L. A. Ocampo Giraldo,²  E. S. Cardenas,²  J. D. Hix,² 
S. J. Thompson,² D. L. Chichester,²  and M. A. Garcés¹ 

¹Hawai'i Institute of Geophysics and Planetology, University of Hawai'i, Mānoa, Hawai'i 96740, USA

²Idaho National Laboratory, Idaho Falls, Idaho 83415, USA

ABSTRACT:

For prompt detection of large (>1 kt) above-ground explosions, infrasound microphone networks and arrays are deployed at surveyed locations across the world. Denser regional and local networks are deployed for smaller explosions, however, they are limited in number and are often deployed temporarily for experiments. With the expanded interest in smaller yield explosions targeted at vulnerable areas such as population centers and key infrastructures, the need for more dense microphone networks has increased. An “attributable” (affordable, reusable, and replaceable) and flexible alternative can be provided by smartphone networks. Explosion signals from a fuel air explosive (thermobaric bomb) and a high explosive with trinitrotoluene equivalent yields of 6.35 and 3.63 kg, respectively, were captured on both an infrasound microphone and a network of smartphones. The resulting waveforms were compared in time, frequency, and time-frequency domains. The acoustic waveforms collected on smartphones produced a filtered explosion pulse due to the smartphone’s diminishing frequency response at infrasound frequencies (<20 Hz) and was found difficult to be used with explosion characterization methods utilizing waveform features (peak overpressure, impulse, etc.). However, the similarities in time frequency representations and additional sensor inputs are promising for other explosion signal identification and analysis. As an example, a method utilizing the relative acoustic amplitudes for source localization using the smartphone sensor network is presented. © 2024 Author(s). All article content, except where otherwise noted, is licensed under a Creative Commons Attribution (CC BY) license (<https://creativecommons.org/licenses/by/4.0/>). <https://doi.org/10.1121/10.0028379>

(Received 26 January 2024; revised 26 June 2024; accepted 11 July 2024; published online 4 September 2024)

[Editor: Yue Ivan Wu]

Pages: 1509–1523

I. INTRODUCTION

Large explosions generate infrasound (<20 Hz) that can travel vast distances. The International Monitoring System (IMS) capitalizes on this phenomenon, using infrasound sensors at monitoring stations around the world to detect large (>1 kt) events (Vergoz *et al.*, 2022). However, for smaller yield explosions, the emitted pressure waves may not be detected by the sparse global network. A solution to this problem is increasing the density of the monitoring network.

On the regional scale there has been success in detecting, locating, and estimating the yield of an explosion caused by an oil spill using infrasound sensors ranging from 340 to 1400 km from the source (Ceranna *et al.*, 2009). Much work has also been done using regional infrasound networks and explosions to improve source localization, investigating propagation effects from weather, and even estimating the atmospheric crosswinds (Modrak *et al.*, 2010; Blixt *et al.*, 2019; Blom, 2023). Additionally, there have been studies of detecting and locating explosions using multiple balloons with infrasound sensors (Bowman and Albert, 2018; Silber *et al.*, 2023; Young *et al.*, 2018).

On the denser local scale, a seismic network (400+ stations) was able to identify various infrasound phases produced by an oil refinery explosion in 2018 (Fuchs *et al.*, 2019). Explosion detection and yield estimation has also been successfully performed using local infrasound networks (Gitterman, 2010; Fee *et al.*, 2021). Overall, the use of these seismic large-N arrays for acoustic explosion analysis including detection, yield estimation, propagation modeling, and source modeling has gained popularity with the advancement of technology that allows for the deployment of hundreds of seismic stations where similar infrasonic stations are still in development (Pasyanos and Kim, 2019; Kim *et al.*, 2021; Kim and Pasyanos, 2023; Chen *et al.*, 2023). However, infrasound and acoustic sensors are still crucial as these seismoacoustic analyses are validated through them. For either case, these local networks are often deployed in the context of experiments or around specific areas of interest (e.g., volcanoes, testing sites).

Smaller yield explosions have been gaining attention with concerns around targeted attacks around power plants, ports, and populated places (Rosoff and Von Winterfeldt, 2007; Biancotto *et al.*, 2020) and with the recent attacks such as the Austin serial bombing in 2018 and the 2020 Nashville bombing. Although not preventative, having a local network for real-time explosion detection could benefit

^{a)}Email: takazaw4@hawaii.edu

the response times to such tragedies and reduce further damage or casualties. However, construction and maintenance of sufficiently dense infrasound or seismic sensor networks across all these areas could prove costly. One way to address this issue is the use of non-traditional sensors such as smartphones.

In the era of Internet of Things (IoT), the use of smartphones as sensors has increased dramatically, especially with the recent developments in mobile crowdsensing (MCS), due to their wide range of built-in sensors (microphone, accelerometer, GNSS, etc.) and their widespread consumer use (Lane *et al.*, 2010; Ganti *et al.*, 2011; Asmar *et al.*, 2019; Capponi *et al.*, 2019). A notable example is the MyShake application which has successfully used data collected on smartphones to create an earthquake early warning system that is currently being used in California, Oregon, and Washington (Kong *et al.*, 2016; Allen *et al.*, 2020). There have also been recent studies using smartphone microphones for monitoring nuclear power plant activities (Eaton *et al.*, 2022; Cárdenas *et al.*, 2023) and for explosion detection (Thandu *et al.*, 2015; Popenhagen *et al.*, 2023). Thus, a smartphone network presents a possible solution to detecting smaller yield explosions. However, it is still important to understand and consider the limitations and strengths of using smartphones as sensors for explosion monitoring. Therefore, we present a comparison of signatures from two-surface explosions captured on an infrasound microphone and on smartphone microphones. The comparison includes representations of the acoustic signal in time, frequency, and time-frequency domains. We also present data from two additional built-in sensors: the barometer and the accelerometer. Additionally, we show a demonstration of source localization using time difference of arrival (TDoA) and amplitude decay methods with the smartphone sensor network data.

Sections IA–IC provide a brief introduction to concepts related to explosions as well as general information on the two explosions. This is followed by an overview of the experimental procedures, features, and representations of the explosion waveforms, and the method used for source localization. Section II first showcases the extracted explosion features from the infrasound microphone, followed by a detailed comparison of data from a co-located infrasound microphone and smartphone microphone, the observed explosion pulse in the other smartphone microphones and built-in sensors, the atmospheric conditions and propagation, and last, the source localization. Sections III and IV summarize our findings and consider the potential of smartphone networks and possible avenues for future research.

A. Explosion terminology

An explosion can be described as a rapid energy release caused by an abrupt increase in volume. The energy released by explosions is often described in TNT (trinitrotoluene) equivalent yield, which is the mass of TNT required to generate the same energy in free air. Explosions can be broadly separated into three categories: high explosive (HE), low

explosive (LE), and nuclear explosive (NE). Explosives are categorized by their reaction speeds and how they generate a pressure wave. Explosion blast waves also have key features such as the maximum pressure of the initial rise (peak overpressure), the time between the initial rise and the fall back to equilibrium (positive pulse duration), and the integral of the overpressure during the positive pulse duration (positive impulse). It is common practice to analyze explosions in reference to a 1 kg TNT equivalent explosion (Kinney and Graham, 1985; Ford *et al.*, 1993; Koper *et al.*, 2002; Garcés, 2019; Schnurr *et al.*, 2020; Kim *et al.*, 2021). This is done by applying scaling laws using the cube root of the TNT equivalent yield, which is known as the scaling factor (Hopkinson, 1915; Craz, 1926; Sachs, 1944; ANSI, 1983; Kinney and Graham, 1985). For example, scaled distance is the true distance between the observer and the source divided by the scaling factor. A deeper dive into the basics of acoustic explosion analysis can be found in Takazawa *et al.*, 2023a, along with an open-source chemical HE dataset.

B. Fuel air explosive

A fuel air explosive (FAE), also known as a fuel air bomb, aerosol bomb, or more broadly as a thermobaric weapon, is a type of LE that works in two steps. A primary explosion releases fine particles of fuel into the air. This is quickly followed by a secondary explosion that ignites the fuel, releasing large quantities of pressure and heat (Klapötke, 2022). Compared to HE with similar yields, FAE generally have a lower peak overpressure and longer pulse duration, resulting in a comparable or larger impulse (Wildegger-Gaissmaier, 2004). The use of FAE has increased rapidly since the first usage in the Vietnam War, despite multiple UN proposals attempting to prohibit the use of these as weapons (Wildegger-Gaissmaier, 2004; Tsybulenko, 2022).

C. The explosions

The two explosions analyzed in this work took place on August 18th, 2022, at the National Security Test Range at Idaho National Laboratory while observers watched from a bunker near the site. The TNT equivalent yields, along with the explosion times are listed in Table I. Since the explosions took place on a rigid surface, the effective yield was doubled to account for ground reflection effects (Kinney and Graham, 1985). Both explosions generated infrasound despite their relatively small yields.

II. METHODS

A. Experimental setup

The explosions were recorded by nine Samsung S22 smartphones running the RedVox application (Garcés *et al.*, 2022) along with a Bruel & Kjaer (B&K) sound level meter type 2250 with the infrasound microphone type 4964. The relative sensor locations and the B&K microphone and smartphones' deployment configurations are shown in Fig. 1.

TABLE I. Explosion type, yield, and time of deflagration or detonation of the recorded explosions in the local time zone and UTC.

Explosion type	TNT ^a Eq. ^b yield (kg)	Effective yield (kg)	Local time (MDT)	Universal time coordinate (UTC)
Fuel air explosive	6.35	12.7	10:05:10	16:05:10
High explosive	3.63	7.26	14:36:41	20:36:41

^aTNT: trinitrotoluene.^bEq.: equivalent.

The smartphones were recording data from the following sensors: microphone, three-axis accelerometer, barometer, and the Global Navigation Satellite System (GNSS) location sensor. A detailed description of the smartphone sensors used by the RedVox application can be found in [Garcés et al. \(2022\)](#). The B&K microphone was placed inside an outdoor pet tent along with the closest smartphone to the explosion. Both the B&K and smartphone microphones were recording at a sample rate of 8000 Hz. The B&K microphone was recording in units of mV that were converted to Pa, whereas the Smartphone microphones were recording in units of bits ([Garcés, 2020, 2023](#)). The other smartphones were placed inside a cylindrical aluminum foil enclosure with a mobile battery pack. This deployment strategy was employed to avoid overheating of the smartphones from direct sunlight while also allowing an open path for the pressure waves to travel.

The phones' distances from the source ranged from 0.87 to 10.99 km as seen in Fig. 1(a), corresponding to scaled distances ranging from 372 to 4711 m/kg^{1/3} for the FAE and from 449 to 5676 m/kg^{1/3} for the HE. The environment surrounding the explosion site was a cold semiarid

desert, with relatively flat topography gradually increasing in elevation with a maximum difference of 75 m at around 11 km from the source. A nearby weather station (~30 km from site) reported temperatures of 24.4 °C for the FAE and 32.2 °C for the HE, an ambient pressure of 84 559 Pa for the FAE and 84 388 Pa for the HE, and winds less than 3 m/s for both explosions. A deeper look into the atmospheric conditions for the explosions will be discussed later.

B. Explosion feature extraction

The standardized (1 kg TNT) explosion features (peak overpressure, positive pulse duration, and positive impulse) were extracted from the B&K infrasound microphone data for a baseline comparison to other high explosive features. The calibrated B&K microphone data were in units of Pa and the three explosion features were extracted using methods described in [Takazawa et al. \(2023a\)](#). The extracted features were compared to a standardized high explosive dataset ([Takazawa et al., 2023b](#)), along with two high explosive feature models from [Kinney and Graham \(1985\)](#) (KG85) and [Schnurr et al. \(2020\)](#) (S20). Although FAE are

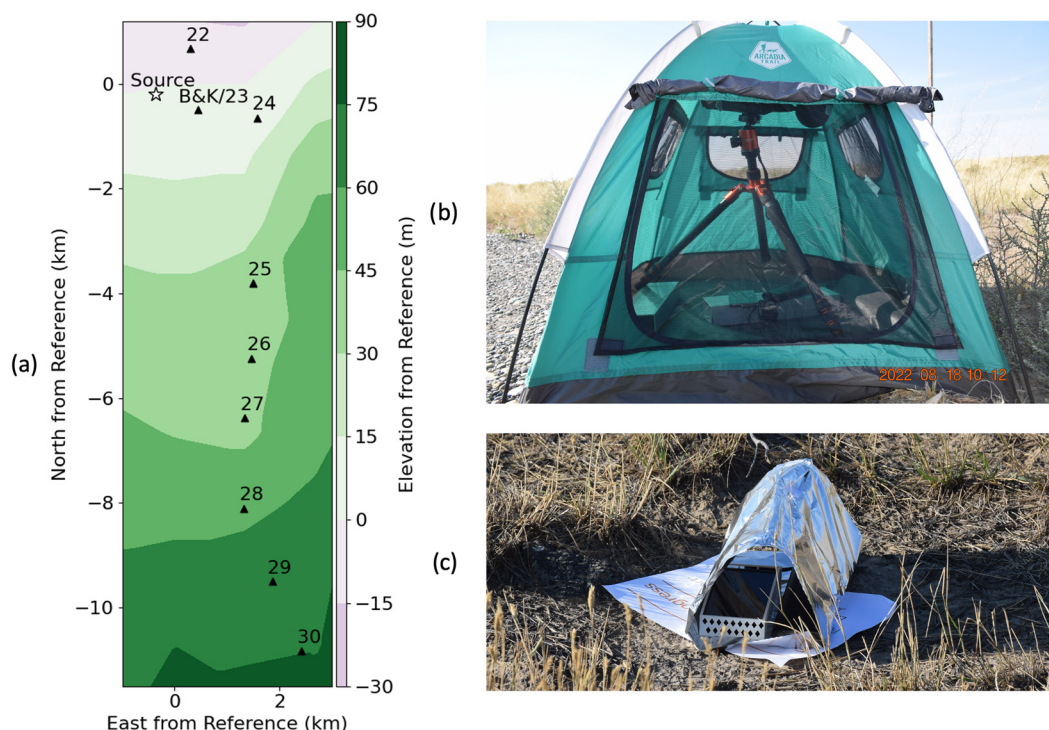


FIG. 1. (Color online) (a) The locations of the sensors (triangles) and source (star) shown with ground elevation in East North UP Coordinates relative to a reference point near the source. The deployment configuration of (b) phone 23 and the B&K microphone and (c) phone 29 (same configuration as the rest of the phones).

not HE, they are included in the comparison to gain some insight on the event and to validate some general trends, such as FAE generally having a longer positive pulse duration than HE.

C. Time, frequency, and time-frequency representations

The comparison of sensor response between the B&K infrasound microphone data and the phone 23 microphone data were done in three domains: time, frequency, and time-frequency. The time comparison was done by observing the normalized time-series of the explosion pulse. The frequency domain comparison was performed by examining two power spectral densities (PSDs), one computed with Welch's method (Welch, 1967) and the other by aggregating the time domain of the Stockwell transform (ST) (Stockwell *et al.*, 1996). For the Welch's method PSD, a Hann window of 1 s length with 50% overlap was used, whereas the ST was constructed with 1/6 octave bands. Similarly, the time frequency domain comparison was done by computing the short time Fourier transforms (STFTs) and STs of the respective waveforms and analyzing the difference in power relative to the maximum. The STFTs were computed with a Hann window of 1 s length with 95% overlap. The increased overlap (>50%) allows for an increase in perceived "resolution" for the benefit of the reader. The STs were computed with the same octave bands used for the PSDs. The time-series were zero-padded to improve amplitude accuracy for all PSDs, STFTs, and STs.

D. Atmospheric conditions and acoustic propagation

The atmospheric conditions play a significant role in acoustic propagation of signals. In addition to the amplitude decay due to geometric spreading of the pressure wave, signals propagating through the atmosphere are affected by frequency dependent attenuation and temperature inversions, which can impact propagation paths and features of the observed signal (Evans *et al.*, 1972; Kim and Rodgers, 2016; Kim *et al.*, 2021; Blom, 2023).

To gain insight on the propagation effects due to atmospheric conditions, we looked at the temperature and wind profiles using the High-Resolution Rapid Refresh (HRRR), an hourly weather forecasting model developed by the U.S. National Oceanic and Atmospheric Administration (Dowell *et al.*, 2022). The expected arrival times were also considered using sound speeds derived from local temperatures.

E. Source localization

Multilateration (MLAT), also called hyperbolic positioning, is a method of locating the source of a signal using the time difference of arrival (TDoA) from time-synchronized sensors. For an acoustic source, this can be achieved by using the speed of sound, the locations of the microphones, and the signal arrival times at said locations. A set of equations can be constructed with these values in terms of relative positions to the source. The equations can

then be solved using various methods, such as Taylor Series (Foy, 1976) or Maximum Likelihoods (Chan and Ho, 1994). A minimum of four sensors are required for 2D MLAT and five sensors for 3D MLAT. However, the number of required sensors is reduced by 1 if we assume a planar arrival. The key advantages of MLAT are that it only requires synchronizations between the sensors and that its computational cost is low, which is ideal for real-time applications such as a smartphone network (Tyagi *et al.*, 2014; Sundar *et al.*, 2018; Mahapatra and Mohanty, 2022a,b).

The source location estimation for the explosion was done with MLAT in 2D by first converting the smartphones' GNSS latitudes and longitudes into east north coordinates. The coordinates and time-corrected arrival times were then used to find location estimates by solving the TDoA equations using least squares optimization. The time correction was performed by using the GNSS times, and relative arrival times were found by cross-correlating the microphone time-series. These estimates were found for all possible sets of three smartphones assuming a planar arrival. The estimates were then further vetted using the ratio of the maximum amplitude across the smartphones with the largest amplitudes (phones 22, 23, and 24). Possible regions for the source location were created using the inverse distance law for attenuation and geometry, assuming an upwardly refracting atmosphere. For example, if the ratio of amplitudes is 1, the set of possible source locations would be the perpendicular line at the midpoint between the two stations, as all points will be equidistant. In contrast, if the ratio was greater or less than 1, the set of possible locations with the same distance ratio (the inverse of the amplitude ratio) will, by Apollonius' definition (Durell, 1923), form a circle. We can use these ratio bounds to exclude any improbable estimates.

III. RESULTS

A. Explosion features of the fuel air explosive and high explosive

The standardized peak overpressure, positive pulse duration, and positive impulse of the FAE and HE are shown in Fig. 2, accompanied by two HE feature models and a HE feature dataset. As stated in the Introduction, we expect to see a smaller peak overpressure, longer positive pulse duration, and an equal or greater positive impulse for the FAE when compared to HE. Overall, the explosion features of the FAE seem to agree with our expectations, except for the peak overpressure value [Fig. 2(a)] being comparable to those of high explosives.

B. The waveforms and power spectral densities of the co-located sensors

The captured FAE and HE waveforms on the B&K infrasound microphone and phone 23 microphone and their representations are shown in Fig. 3. From initial observation of the normalized amplitudes, we see a drastic difference in the shape of the waveform timeseries [Figs. 3(a) and 3(d)].

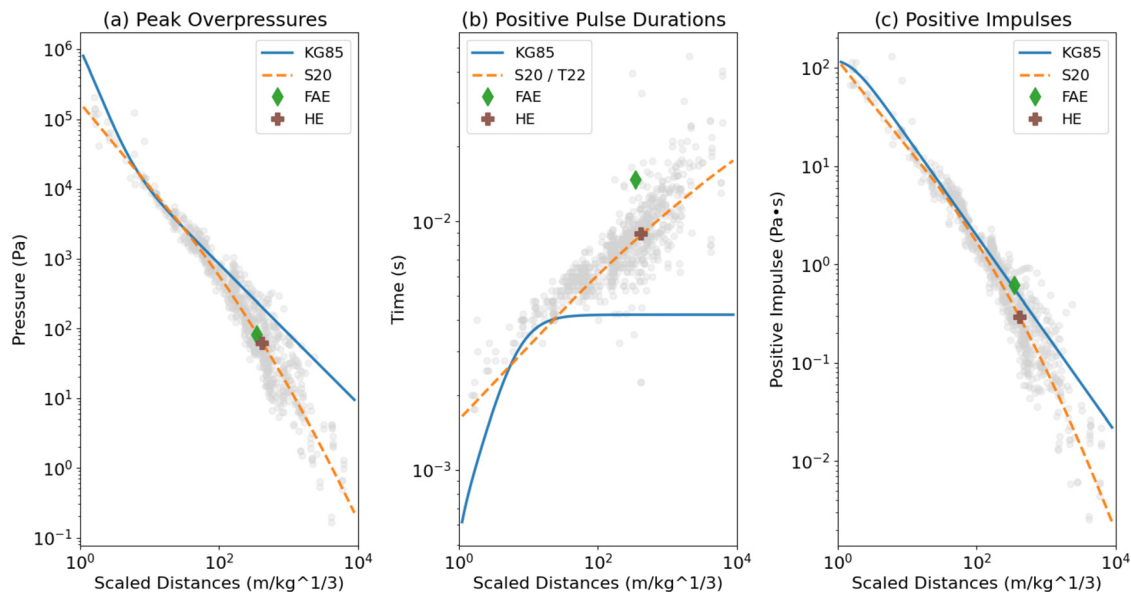


FIG. 2. (Color online) The standardized (1 kg TNT) explosion features of HE (gray circles) from Takazawa *et al.* (2023b), the FAE (green diamond), and the HE (brown plus sign) accompanied by notable explosion feature models of (a) peak overpressures, (b) positive pulse durations, and (c) positive impulses.

Where the B&K shows the clear explosion pulse that we expect, the smartphone shows a distorted pulse with a significantly shorter positive pulse duration and larger pressure spike after the onset. These differences make analysis by extracting explosion pulse features difficult without heavy processing. However, there are still similarities, such as the duration of the whole pulse (time between onset and

equilibrium) and locations of small perturbations seen in the pulse (i.e., high frequency content). The distortions of the smartphone data are most likely from the diminishing frequency response and phase shifts at infrasound ranges (<20 Hz) for smartphone microphones (Asmar *et al.*, 2019; Slad and Merchant, 2021). We see this effect more clearly in the frequency domain.

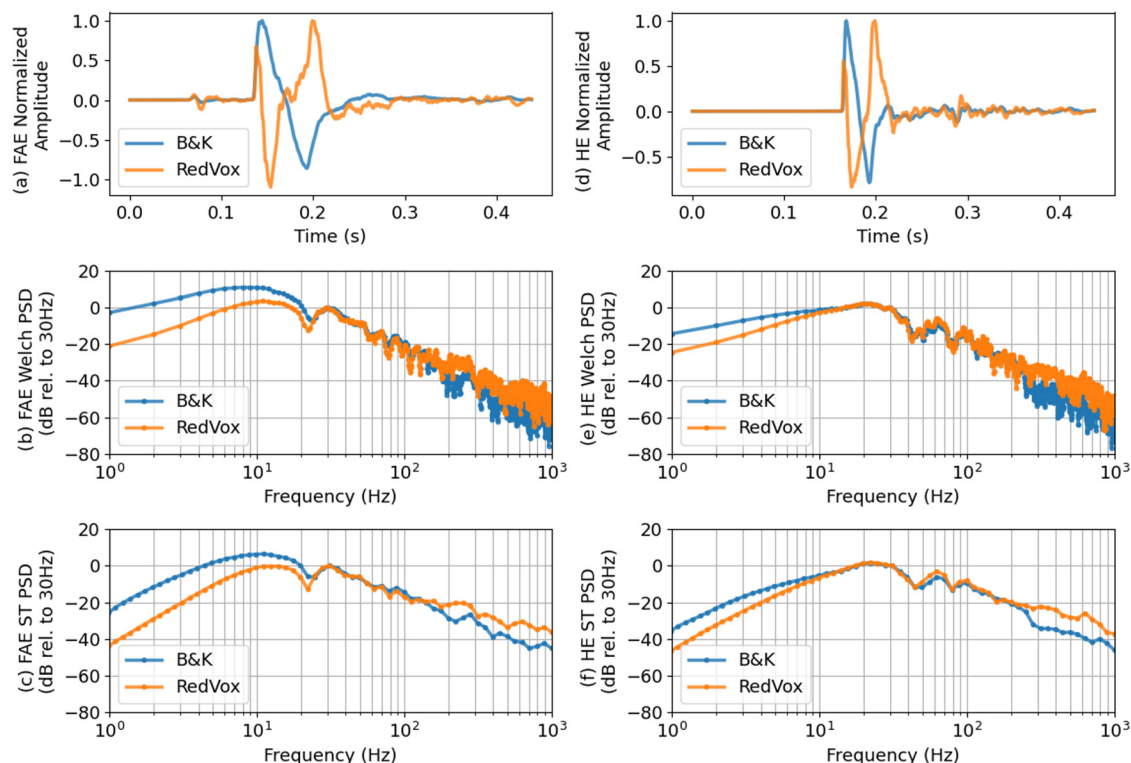


FIG. 3. (Color online) The (a), (d) normalized time series of the explosion pulse for the B&K (darker blue) and the smartphone (lighter orange). The power spectral density of the B&K and the smartphone using (b), (e) Welch's method and (c), (f) the S-transform, both of which are displayed in decibels relative to 30 Hz.

The PSDs calculated with Welch's method and the ST show similar patterns between the smartphone and B&K microphone, unlike what we saw with the waveforms. The PSDs are normalized to the 30 Hz value and shown in units of decibels for ease of comparison. Focusing on the B&K PSDs, we see that the maximum signal energy concentration is similar for the Welch's and ST methods, around 10 Hz for the FAE and around 20 Hz for the HE. For the smartphone PSDs, we see a similar energy concentration to the B&K for the HE, however, at a smaller magnitude at the 10 Hz peak for the FAE. As mentioned previously, the frequency response of the smartphone's onboard microphone drastically tapers off in the infrasound range (<20 Hz), which causes this discrepancy. It is possible to correct for the frequency response of the smartphone microphone signals (Asmar *et al.*, 2019) and allow for explosion analysis using feature extraction methods. However, this is beyond the scope of this paper as it requires additional experimentation to accurately determine each smartphone's frequency response.

C. The time frequency representations of the co-located sensors

The time frequency representations (TFRs) of the explosion pressure waves were scaled in decibels relative to their maximum value as seen in Fig. 4 for the FAE and Fig. 5 for the HE. Any values that were less than -12 dB (6.25% of the maximum power) were masked as -12 dB to reduce noise and increase ease of viewing. On initial observation of the STFTs, we see that the energy of the explosion pulse concentrates around 10 Hz for the FAE [Fig. 4(a),

4(b)] and around 20 Hz for the HE [Figs. 5(a) and 5(b)], matching the PSD results. The smartphone spectra show less power for the lower frequency range due to the diminishing frequency response as previously discussed. We also see more energy visible in the 30 to 60 Hz range compared to the B&K STFTs, since the representations are relative to the maximum power. The difference plots [Fig. 4(c) and 5(c)] highlight these effects clearly, showing that the power at the frequency of peak energy concentration was nearly identical between the two sensors, with a difference within 3 decibels ($\sim 50\%$) for the FAE and nearly imperceptible for the HE.

In contrast to the rectangular or cocoon-like shape of the STFTs, the STs have a cone-like shape with two high energy regions separated by a lower-energy region around 20 to 30 Hz for the FAE and 40 to 50 Hz for the HE. Although this gap in the high-energy region is also present in the STFTs, the power of the higher frequency high-energy region relative to the maximum was smaller, especially for the B&K, for which the power in the higher frequency region did not make the -12 dB threshold [Figs. 4(a) and 5(a)]. The cone-like shape is an inherent characteristic of the ST for transient signals (i.e., shock waves), as the time windows get broader for lower frequencies. Comparing the difference plots, we see that the STs contain more regions of similarity (power difference of <3 dB) since they have much higher resolution in the time domain, due to the shape of the time-frequency bins varying with frequency. Because of this increase in resolution in the time domain for higher frequencies and in the frequency domain in the lower frequencies, STs may be more beneficial in this case, despite

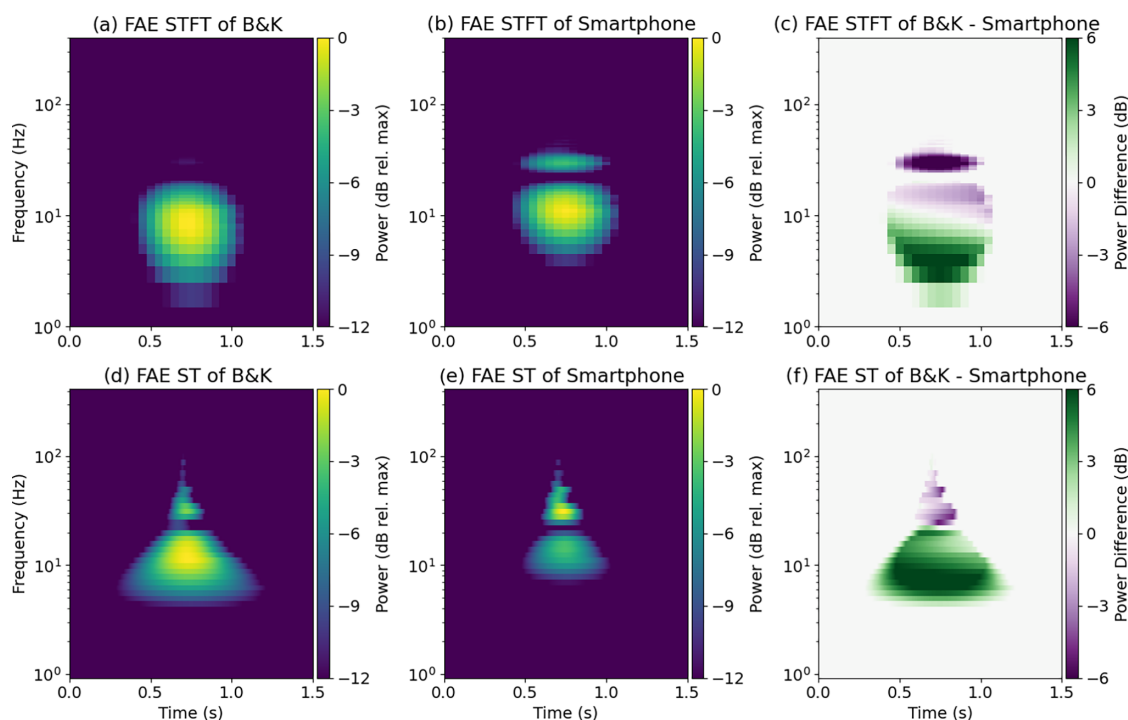


FIG. 4. (Color online) The normalized STFT of the FAE waveform, shown in decibels relative to the maximum of (a) the B&K microphone data, (b) the smartphone microphone data, and (c) the difference between the two STFTs. The normalized Stockwell Transform of the FAE waveform, shown in decibels relative to the maximum of (d) the B&K microphone data, (e) the smartphone microphone data, and (f) the difference between the two STs.

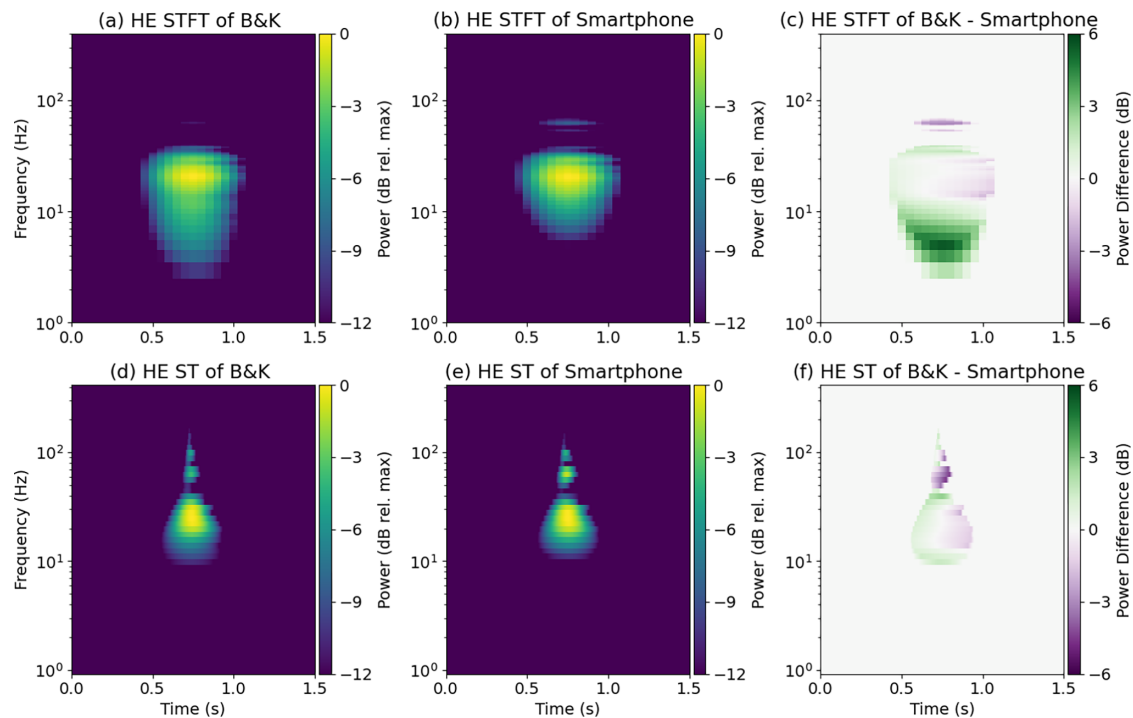


FIG. 5. (Color online) The normalized STFT of the HE waveform, shown in decibels relative to the maximum of (a) the B&K microphone data, (b) the smartphone microphone data, and (c) the difference between the two STFTs. The normalized Stockwell Transform of the HE waveform, shown in decibels relative to the maximum of (d) the B&K microphone data, (e) the smartphone microphone data, and (f) the difference between the two STs.

their greater computational cost compared to STFTs. Overall, the TFRs of the explosion signals for the co-located sensors show, like the PSDs, greater similarity than the waveforms for both the FAE and the HE. Unlike the PSDs, however, TFRs have the added benefit of the time information, which is more useful in analysis methods that require concise arrival times.

D. The other sensors and smartphones

The FAE and HE signals captured in the smartphone arrays from the various sensors are shown in Figs. 6 (FAE) and 7 (HE), with each timeseries normalized to the largest amplitude among all the stations. The smartphones are listed, from top to bottom, in descending distance to the

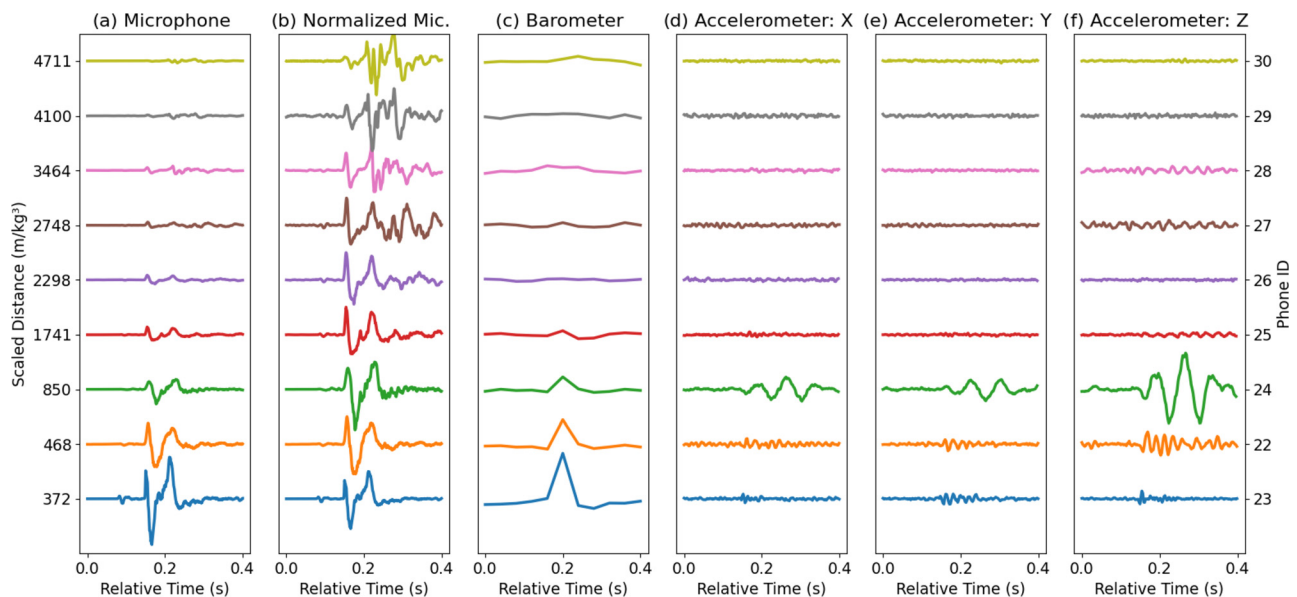


FIG. 6. (Color online) Plots of the FAE waveforms collected by each of the deployed smartphones' (a) microphone, (b) normalized microphone, (c) barometer, (d) x axis accelerometer, (e) y axis accelerometer, and (f) z -axis accelerometer. Amplitudes in each panel, except (b), are shown relative to the maximum value of all the waveforms to highlight attenuation effects. Amplitudes in panel (b) are shown relative to each waveform's maximum value. The left-hand y axis ticks show the scaled distances of the smartphones and the right-hand y axis ticks show the smartphones' IDs. The effects of propagation can be seen to affect the pulse shape in the (b) normalized microphone graphs.

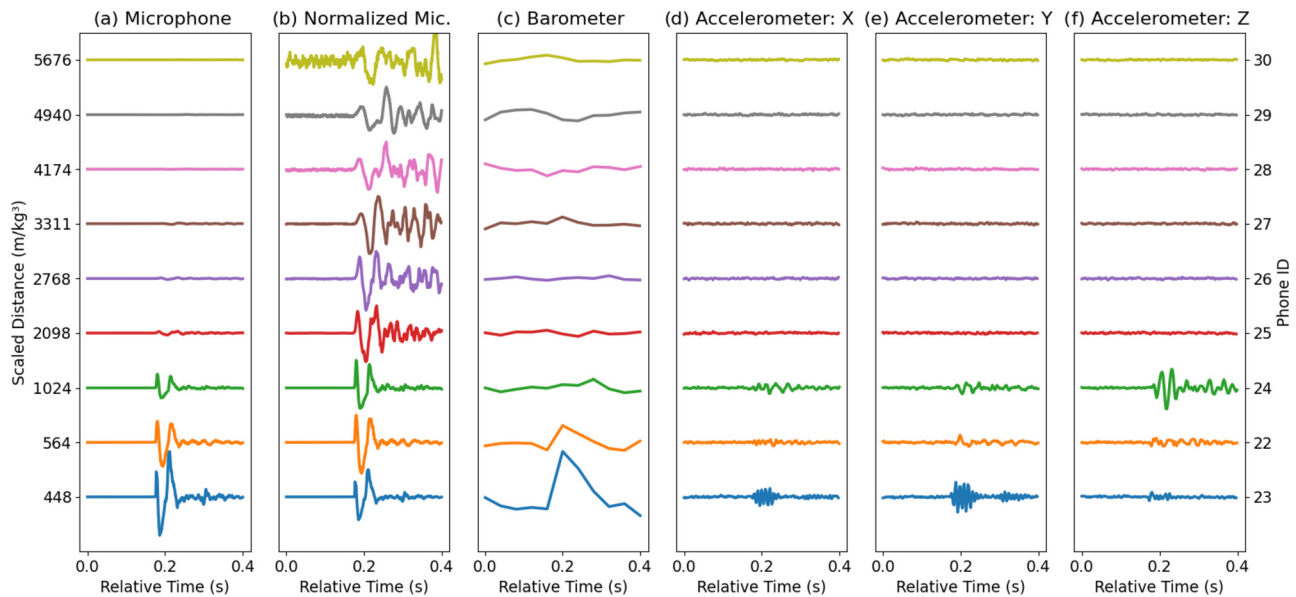


FIG. 7. (Color online) Plots of the HE waveforms collected by each of the deployed smartphones' (a) microphone, (b) normalized microphone, (c) barometer, (d) x axis accelerometer, (e) y axis accelerometer, and (f) z axis accelerometer. Amplitudes in each panel, except (b), are shown relative to the maximum value of all the waveforms to highlight attenuation effects. Amplitudes in panel (b) are shown relative to each waveform's maximum value. The left-hand y axis ticks show the scaled distances of the smartphones and the right-hand y axis ticks show the smartphones' IDs. The effects of propagation can be seen to affect the pulse shape in the (b) normalized microphone graphs.

source and are equally spaced on the y axis regardless of their scaled distance. Focusing on the microphone data, we see the effects of propagation, namely differences in amplitude [Figs. 6(a) and 7(a)] and pulse shape [Figs. 6(b) and 7(b)], increasing as we move away from the source as expected. Additionally, for the FAE [Figs. 6(a) and 6(b)], we can see a precursory signal from the HE initiator before the main onset.

For the barometer, we have a clear signal from the source up to phone 25 for the FAE (scaled distance of $1741 \text{ m/kg}^{1/3}$) and up to phone 22 for the HE (scaled distance of $564 \text{ m/kg}^{1/3}$). The barometer sensor's uneven sampling rate averages to about 25 Hz, which is much lower than the sampling rates of the other sensors. This contributes to the lower level of detail in the shape of the pulse since the higher frequency components of the signal are not present. This also means that without the presence of infrasound, we do not expect the barometer to record a signal, which explains the discrepancy between the FAE [Fig. 6(c)] and HE [Fig. 7(c)] at similar scaled distances since the frequency concentration of the HE signal is higher. Like the barometer, the accelerometer is also unevenly sampled, however its sampling rate is faster, averaging to about 420 Hz.

The motions captured in the accelerometer are from the same time as the microphone data, so they are most likely from the air-to-ground interaction of the acoustic pressure wave and not the ground waves generated by the explosion. Phone 24 was placed near a concrete structure supporting a flagpole that may have resonated with the low frequency of the signal, which would explain the larger amplitude and period seen in the FAE and slightly less in the HE. The smaller amplitude in Phone 23 compared to 22 for the FAE

signal may be due to 23 being placed inside a tent and/or from the difference in stability of the ground, as phone 22 was placed in an area with coarser gravel compared to phone 23.

The STs of the microphone data from all nine smartphones are presented in Fig. 8 for the FAE and Fig. 9 for the HE. As in Figs. 4 and 5, each ST is scaled to decibels relative to its maximum value with a mask applied for any values less than -12 dB . At a quick glance we see that the STs have a clear cone shape up to phone 26 for the FAE and up to phone 24 for the HE after which they are distorted due to the aforementioned attenuation effects. This agrees with what we see in the microphone waveforms and is expected as the FAE has greater energy and a lower central frequency. For the STs of the mid-range phones (phones 25 to 27), we see the expected greater effects of the attenuation on higher frequencies as the greatest concentration of power appears to be shifting to a lower frequency. However, looking at the farthest phones (phones 28 to 30) we see that the greater concentration of power is higher in frequency than the other STs. This could be due to the frequency response of the phones and/or propagation effects, although a more thorough investigation including detailed propagation modeling would be required to state this conclusively.

E. Atmospheric conditions and propagation of the explosions

The hourly atmospheric profiles of the temperature and wind containing the time of each explosion along with the effective sound speeds calculated with the temperature and wind data are shown in Figs. 10 and 11. Comparing the temperature profiles for the FAE and the HE [Figs. 10(a) and

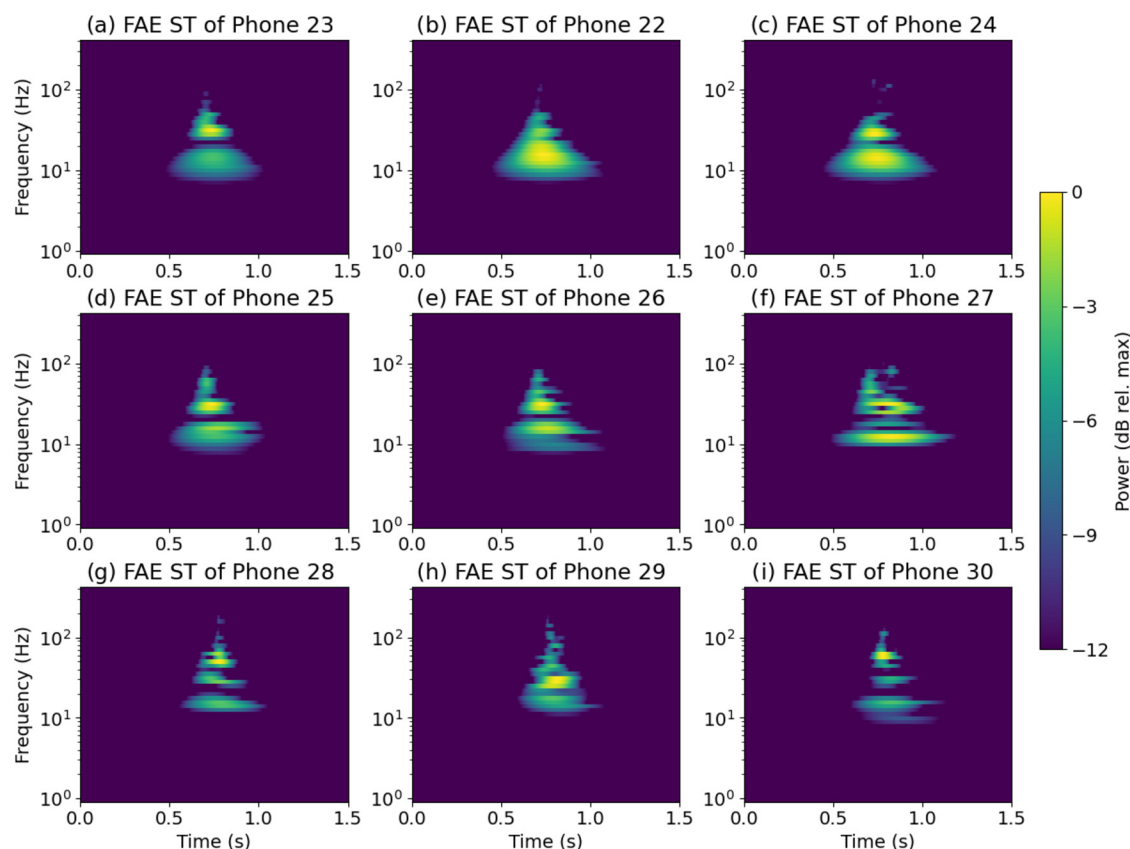


FIG. 8. (Color online) The ST of the FAE signals captured on the smartphone microphones. The individual figures are organized from (a) closest to (i) farthest from the source.

11(a)], we see that temperatures for the FAE were near vertical for lower elevations since event took place later in the morning and the temperature inversion was waning. Although the hourly snapshots of the temperature profiles are not quite inverted for the FAE, the atmosphere can change rapidly on a short time scale and affect the expected amplitude (Bush *et al.*, 1997; Kulichkov, 1998; Kulichkov and Bush, 2001; Carmichael *et al.*, 2022; Averbuch *et al.*, 2022). However, determining the extent of its effect is beyond the scope of this paper.

Moving to the wind profiles for the explosion events [Figs. 10(b), 10(c), 11(b), 11(c)], we see that it was a relatively calm day with wind speeds not exceeding 5 m/s. This is more apparent when looking at the calculated effected sound speed profiles [Figs. 10(d), 10(e), 11(d), and 11(e)], as it closely follows the temperature profile with slight variations. To investigate the extent of wind effects on arrival times, the smartphone waveforms were vertically stacked by distance to source along with sound speeds calculated by the temperatures recorded by the nearby weather station (Fig. 12). Looking closely at phone 22 for the FAE [Fig. 12(a)], we see that intersection between the onset of the explosion pulse and the sound speed line is not as close as the other phones in the network. Since phone 22 is the only phone located north of the explosion source, this delay in arrival time could be due to the north-south winds, as it would create an effective sound speed difference around -4 m/s. If

this were the case, we would expect to see phone 22's arrival time to be earlier than the other phones for the HE, since the wind direction had reversed creating an effective sound speed difference around $+4$ m/s. However, upon inspection of the HE propagation [Fig. 12(b)], we find that onset of the explosion pulse for phone 22 and sound speed line to be near and not earlier for phone 22. Additionally, phone 22's discrepancy in arrival time could be affected by local terrain, as it is the only phone located below the source in elevation. Thus, whether winds caused the delay in arrival time of the FAE explosion pulse for phone 22 would be inconclusive. However, looking at the sound speeds and explosion waveform onsets in the other phones for both explosions we see a close match. Hence, the overall effect of the wind on the arrival times of the explosion pulse are most likely negligible when looking at the additional phones.

F. Source localization of the fuel air explosive

The source locations estimated using 2D MLAT from all possible sets of three stations are seen in Fig. 13(a), along with the associated hyperbolas. Although most of the estimates are near (<1 km) the actual source, there are a few dozen that scattered farther out, including some estimates beyond the scope of the figure (>100 km). Limiting the estimates to be within 15 km (local range) of the smartphone network, the mean of the source estimates would be located

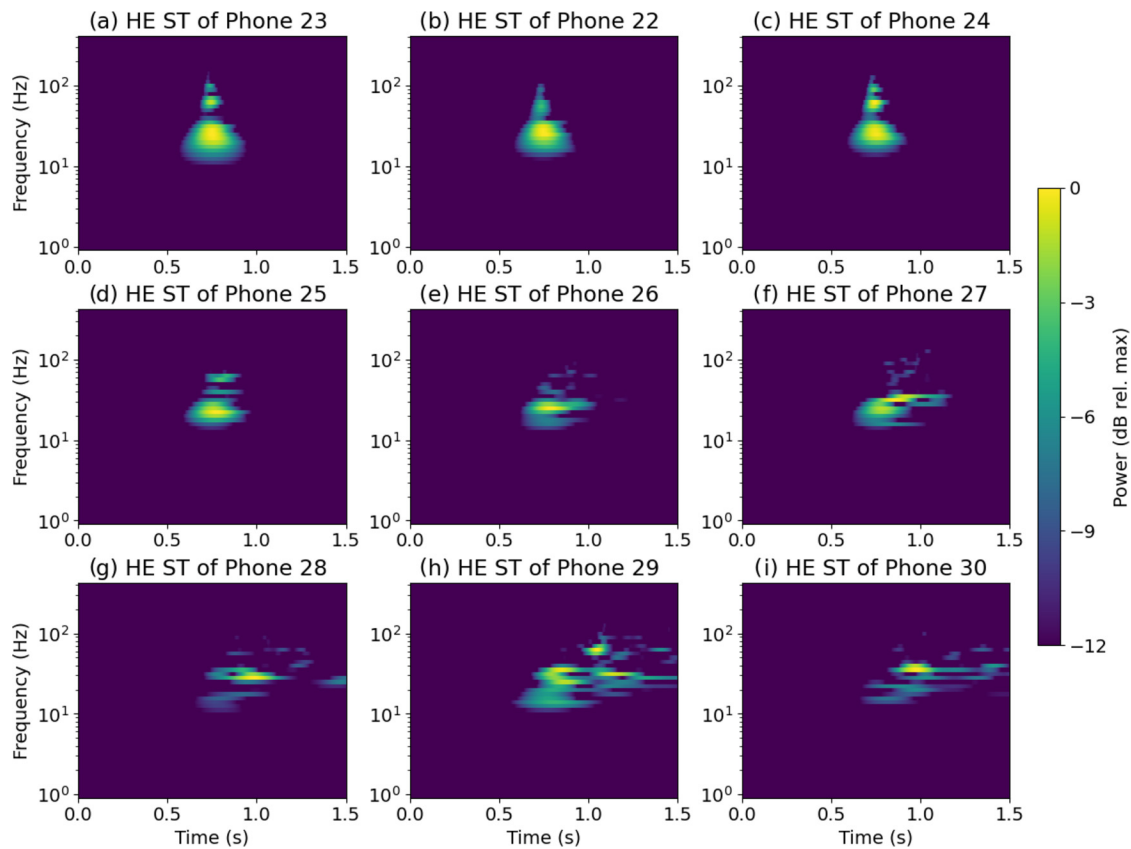


FIG. 9. (Color online) The ST of the HE signals captured on the smartphone microphones. The individual figures are organized from (a) closest to (i) farthest from the source.

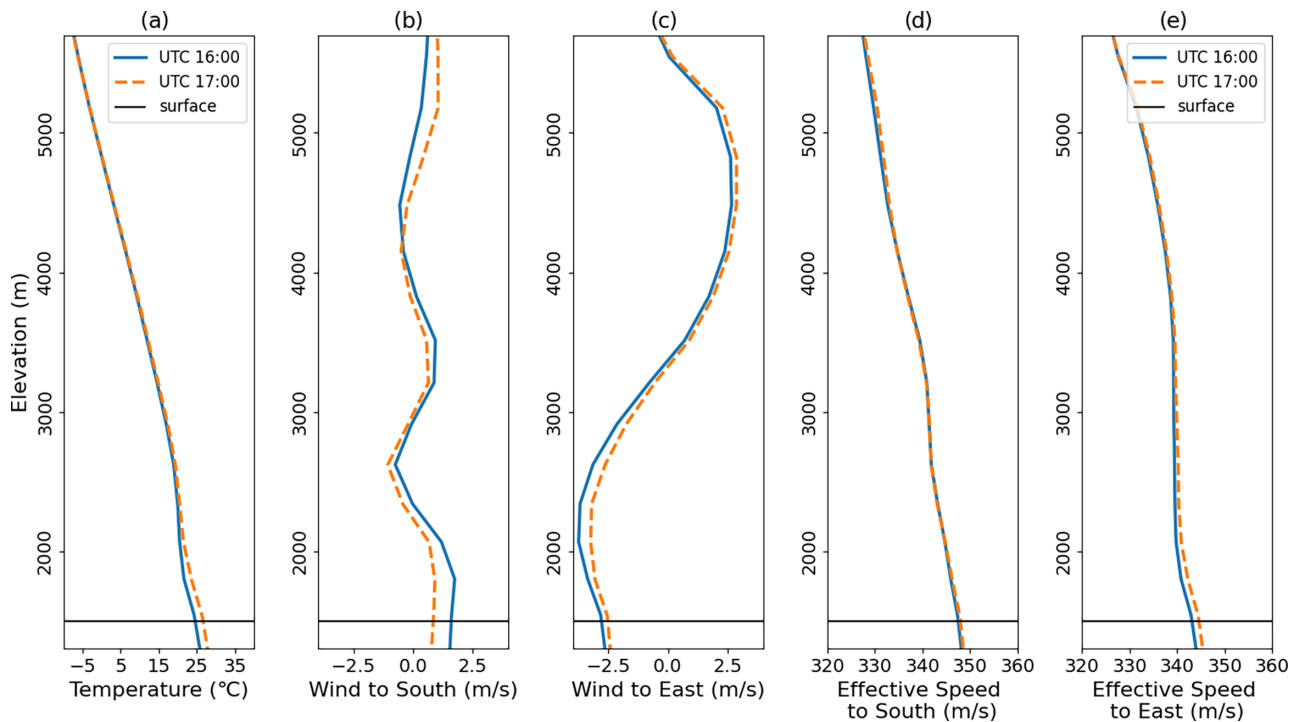


FIG. 10. (Color online) Atmospheric profiles for (a) temperature, (b) winds due south, (c) winds due east, (d) effective sound speeds due south, and (e) effective sound speeds due east. The effective sound speeds were calculated from the temperature and wind data. Data before (solid line) and after (dashed line) the fuel air explosive deflagration (UTC 16:05) obtained using the high-resolution rapid-refresh (HRRR). The horizontal black line indicates the elevation at the explosion source.

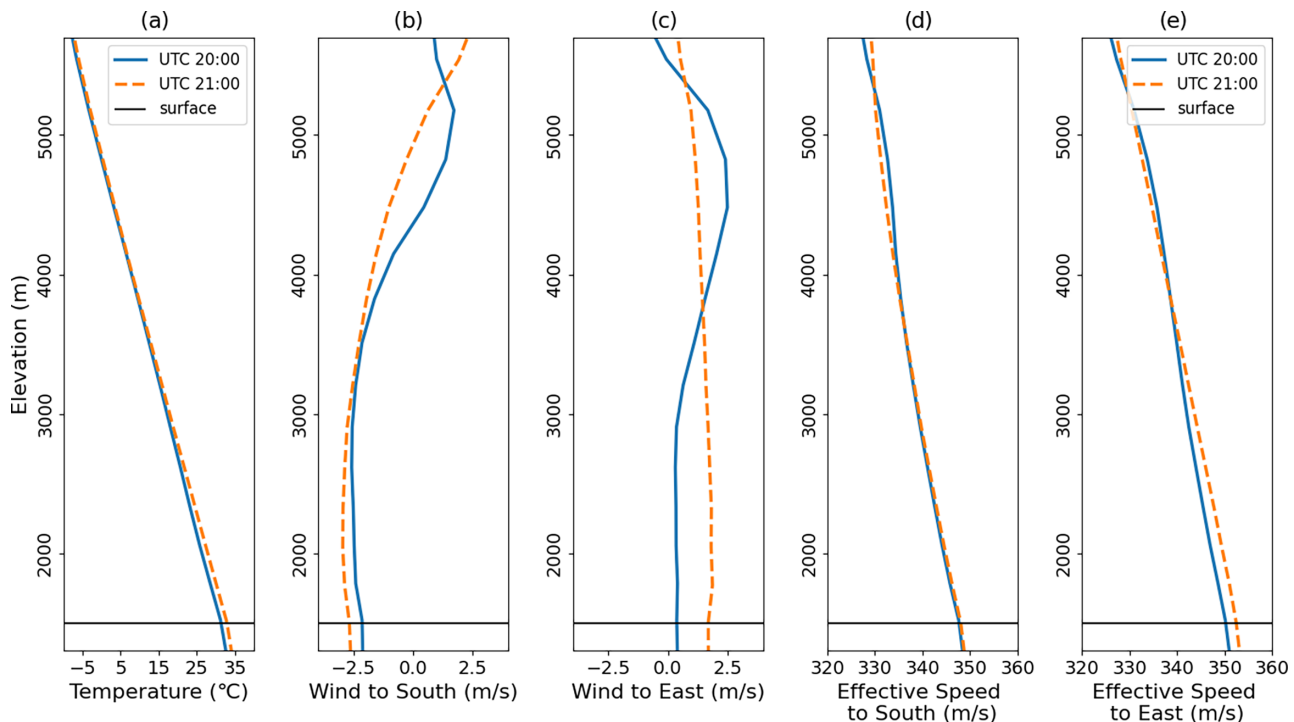


FIG. 11. (Color online) Atmospheric profiles for (a) temperature, (b) winds due south, (c) winds due east, (d) effective sound speeds due south, and (e) effective sound speeds due east. The effective sound speeds were calculated from the temperature and wind data. Data before (solid line) and after (dashed line) the high explosive detonation (UTC 20:36) obtained using the HRRR. The horizontal black line indicates the elevation at the explosion source.

462 m from the source and the median would be located 127 m from the source. However, the standard deviation of the estimates would be 1218 m in the east-west direction and 2064 m in the north-south direction, which would be too large to be a confident result. These widely varying source estimates are likely a side effect of how the smartphones were deployed. Many of the sets form a straight line, which

affects the performance of 2D MLAT by having the hyperbolas overlap each other in many locations. To improve both accuracy and confidence, we utilize geometry and the aforementioned inverse distance law to exclude the “bad” estimates using the three phones (22, 23, and 24) with the largest amplitudes in the microphone and barometer. By computing the amplitude ratios of the microphone data and

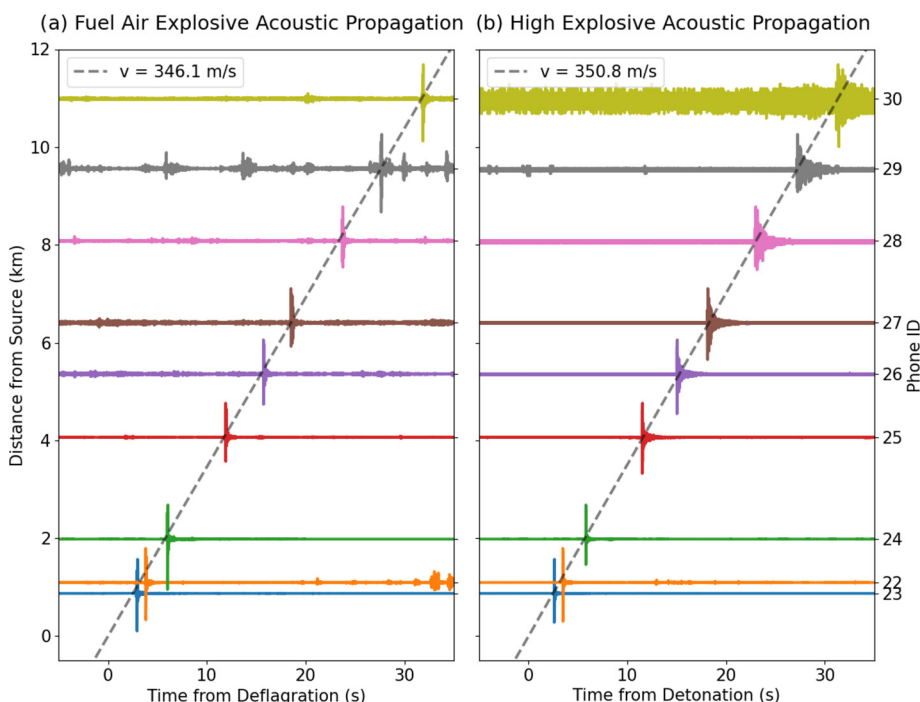


FIG. 12. (Color online) The normalized smartphone acoustic waveforms of (a) the FAE and (b) the HE plotted relative to the distance from the explosion source. Sound speed (gray dashed line) calculated from temperatures recorded at the local weather station is shown for reference.

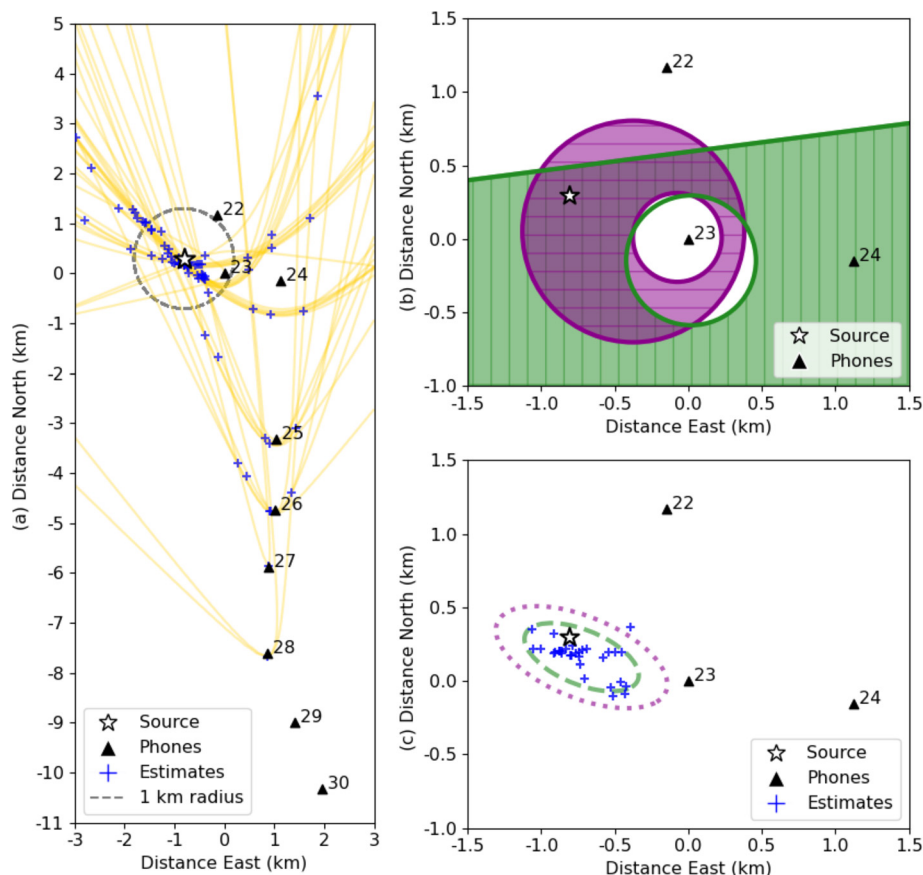


FIG. 13. (Color online) (a) The source estimates (blue crosses) along with the hyperbolas (yellow lines) associated with each phone station pair and a 1 km radius from the source (gray dashed line) for reference. (b) Possible range of sources inferred from signal amplitude ratios from phone 22 and 23 (green vertical lines) and phone 23 and 24 (purple horizontal lines). (c) The vetted source estimates and the confidence intervals at 95% (green dashed) and 99% (purple dotted). The distances listed are relative to phone 23.

barometer data across the phones, we were able to set bounds for possible locations of the source.

The computed ratios between phones 22 and 23 were 2.00 for the microphone and 2.18 for the barometer with phone 23 being the larger of the pair. Using these values, we set boundaries for an amplitude ratio of 1 and 3. The larger boundaries for the amplitude ratios were selected to accommodate for the uncertainty in the calculated values and for potential variations in the frequency response across the smartphones (Asmar *et al.*, 2019). By taking the inverse of the amplitude ratios, we set the distance ratio boundaries to be 1 and 1/3. The distance ratio of 1 forms the green line and the distance ratio of 1/3 forms the green circle (by Apollonius's definition) seen in Fig. 13(b). The region within these boundaries is shaded with vertical green lines. Similarly, we computed the amplitude ratio to find the distance ratio between phones 23 and 24. The amplitude ratios were 4.20 for the microphone and 2.97 for the barometer, which we used to set bounds for amplitude ratios of 2 and 5, forming the two purple circles in Fig. 12(b). The region within these boundaries is shaded with horizontal purple lines. Using these four boundaries, the 84 estimates were reduced to the 31 seen in Fig. 13(c). The mean east north coordinates of the final estimates were found to be 160 m from the source and the 95% confidence ellipse (dashed) has a semi-minor axis of 231 m and a semi-major axis of 389 m, giving an area of 0.28 km². The 99% confidence ellipse (dotted) has a semi-minor axis of 346 m and a semi-major axis of 582 m giving an area of 0.63 km².

IV. DISCUSSION AND CONCLUSIONS

An array of nine smartphone sensors in an open field spanning 0.87 to 10.99 km from the source captured signals from a fuel air explosive and a high explosive. The closest smartphone to the source was accompanied by an infrasound microphone to compare the waveform and its representations.

We found that the co-located smartphone microphone data recorded a filtered explosion pulse compared to the infrasound microphone due to the smartphone microphone's diminishing frequency response and associated phase shift at low frequencies. This filtered waveform makes explosion analysis using explosion features such as peak overpressure, positive pulse duration, or impulse difficult without correcting for the smartphone's frequency response. In the context of mobile crowdsensing (MCS), this may prove difficult as every phone in the network would need to be tested for their frequency response as they can vary by phone model and even between individual phones of the same model. Additionally, the average smartphone user would likely not have the equipment or knowledge necessary to perform such test.

Looking at the frequency representations, we saw that the overall shapes of the PSDs match, but the magnitudes differing in the infrasound range (below 20 Hz), aligning with previous smartphone microphone studies. Similarly, the TFRs of the explosions showed clear visual similarities in shape despite the expected difference in power. Both frequency and time-frequency representations could prove useful by analyzing the similarities between these representations and those of

traditional explosion data. The time-frequency representations (STs) have the additional benefit of finer time resolution compared to the frequency representations.

Comparing multimodal data from the additional smartphones, we saw that the microphone signal was clearly recorded for all phones in the network, and both the accelerometer and barometer had recorded signals associated with the explosion pressure wave arrival for the closer phones. These additional sensors could prove useful as additional verification for explosion detection. However, future investigation would be required to verify this. Although the accelerometer did not seem to capture ground motion associated with the explosion for either the FAE or the HE, further research using below surface explosions may be fruitful as they create stronger ground motion. The STs of the acoustic waveforms showed similarity between the phones for the closer stations for both the FAE (<6 km) and the HE (<2 km). The farther phones (>8 km) showed either an amplification of higher frequencies or an attenuation of the lower frequencies in the STs, depending on the phone. This phenomenon requires further investigation using methods such as propagation modeling and attenuation modeling.

We also presented an example of source localization for the FAE with the smartphone network using a 2D MLAT method, which is ideal for real-time applications due to its simplicity and low computational cost. The majority of the source estimates were within 1 km of the actual source with the mean and median estimates being 462 and 127 m away from the source, respectively, however the standard deviation of the estimates was significantly larger creating a low precision result. To address this issue, the collection of source estimates was further refined using amplitude decay relations and the three phones with the largest amplitudes, resulting in a 95% confidence ellipsis with an area of 0.28 km² and mean value 160 m from the source. However, the presented source localization methods did not consider the propagation effects from atmospheric conditions or local geometries. Since TDoA methods depend on having precise constant sound speeds and there was some wind present, this could affect the accuracy of the source estimate. Furthermore, the methods using amplitude ratios to refine the source estimates may not be viable under different atmospheric conditions or at locations with complex local geometries (i.e., urban areas). Thus, implementing accurate source localization on real time applications would require more research and will be investigated in future works.

All in all, compared to the infrasound microphone data, the smartphone microphone data captured a high-passed waveform of the explosion pulse due to its diminishing frequency response below 20 Hz. Although it is possible to deconvolve an unfiltered signal from the smartphone microphone data, it would require accurate knowledge of the individual microphones' responses. Additionally, the similarities between the infrasound microphone data and the smartphone microphone data in the frequency and time-frequency domain may be sufficient for explosion detection and analysis without deconvolution. The smartphones'

additional sensors may also provide opportunities for new methods to be developed. Although having a permanent dense infrasound microphone network in key locations would be ideal, the associated costs may be too great to overcome. In contrast, a smartphone network could be deployed and maintained at significantly lower cost. In conclusion, having a dense network of smartphones could be beneficial in key locations, and would add to the current arsenal of sensors used for explosion monitoring.

ACKNOWLEDGMENTS

The authors are grateful for the support from the U.S. Department of Energy, National Nuclear Security Administration, Office of Defense Nuclear Nonproliferation, Research and Development. The contributions of S.K.T., S.K.P., and M.A.G. were supported by the Department of Energy National Nuclear Security Administration under Award Nos. DE-NA0003920 (MTV) and DE-NA0003921 (ETI). This was performed in part under the auspices of the U.S. Department of Energy by the Idaho National Laboratory (INL). The authors would also like to thank the editor Yue Ivan Wu, reviewer Daniel Bowman, and three anonymous reviewers for the extensive and thorough feedback which has expanded and improved this article.

AUTHOR DECLARATIONS

Conflict of Interest

The authors state that they have no conflicts to disclose.

DATA AVAILABILITY

The data used for this research are available as a pandas DataFrame (The pandas development team, 2024), a collection of SAC files (Goldstein *et al.*, 2003; Goldstein and Snoke, 2005), and a collection of miniSEED files (Ahern *et al.*, 2009) for greater usability. The data can be found in the Harvard Dataverse open-access repository with the following Digital Object Identifier doi:10.7910/DVN/XK6GUC (Takazawa *et al.*, 2024).

- Ahern, T., Casey, R., Barnes, D., Benson, R., Knight, T., and Trabant, C. (2009). "SEED reference manual," version 2.4, Incorporated Research Institutions for Seismology, Washington, DC, http://www.fdsn.org/pdf/SEEDManual_V2.4.pdf (Last viewed August 22, 2024).
- Allen, R. M., Kong, Q., and Martin-Short, R. (2020). "The MyShake platform: A global vision for earthquake early warning," *Pure Appl. Geophys.* **177**, 1699–1712.
- ANSI (1983). *S2-20: Estimating Air Blast Characteristics for Single Point Explosions in Air, With a Guide to Evaluation of Atmospheric Propagation and Effects* (American National Standard Institute, Washington, DC).
- Asmar, K., Garcés, M. A., and Williams, B. (2019). "A method for estimating the amplitude response of smartphone built-in microphone sensors below 4 kHz," *J. Acoust. Soc. Am.* **146**(1), 172–178.
- Averbuch, G., Ronac-Giannone, M., Arrowsmith, S., and Anderson, J. F. (2022). "Evidence for short temporal atmospheric variations observed by infrasonic signals: 1. The troposphere," *Earth Space Sci.* **9**(3), e2021EA002036.
- Biancotto, S., Malizia, A., Pinto, M., Contessa, G. M., Coniglio, A., and D'Arienzo, M. (2020). "Analysis of a dirty bomb attack in a large

- metropolitan area: Simulate the dispersion of radioactive materials,” *J. Inst.* **15**(2), P02019.
- Blixt, E. M., Näsholm, S. P., Gibbons, S. J., Evers, L. G., Charlton-Perez, A. J., Orsolini, Y. J., and Kvaerna, T. (2019). “Estimating tropospheric and stratospheric winds using infrasound from explosions,” *J. Acoust. Soc. Am.* **146**(2), 973–982.
- Blom, P. (2023). “Regional infrasonic observations from surface explosions-influence of atmospheric variations and realistic terrain,” *Geophys. J. Int.* **235**(1), 200–215.
- Bowman, D. C., and Albert, S. A. (2018). “Acoustic event location and background noise characterization on a free flying infrasound sensor network in the stratosphere,” *Geophys. J. Int.* **213**(3), 1524–1535.
- Bush, G. A., Kulichkov, S. N., and Svertilov, A. I. (1997). “Some results of the experiments on acoustic wave scattering from anisotropic inhomogeneities of the middle atmosphere,” *Izv. Atmos. Oceanic Phys.* **33**(4), 445–452.
- Cárdenas, E. S., Takazawa, S. K., Garcés, M. A., Chichester, D. L., Hunley, R. D., and Young, C. D. (2023). “An assessment of persistent acoustic monitoring of a nuclear reactor during full power generation,” *Acoustics* **5**(2), 429–443.
- Carmichael, J. D., Thiel, A. D., Blom, P. S., Walter, J. I., Dugick, F. K. D., Arrowsmith, S. J., and Carr, C. G. (2022). “Persistent, ‘mysterious’ seismoacoustic signals reported in Oklahoma state during 2019,” *Bull. Seismol. Soc. Am.* **112**(1), 553–574.
- Capponi, A., Fiandrino, C., Kantarci, B., Foschini, L., Kliazovich, D., and Bouvry, P. (2019). “A survey on mobile crowdsensing systems: Challenges, solutions, and opportunities,” *IEEE Commun. Surv. Tutorials* **21**, 2419–2465.
- Ceranna, L., Le Pichon, A., Green, D. N., and Mialle, P. (2009). “The Buncefield explosion: A benchmark for infrasound analysis across Central Europe,” *Geophys. J. Int.* **177**(2), 491–508.
- Chan, Y. T., and Ho, K. C. (1994). “A simple and efficient estimator for hyperbolic location,” *IEEE Trans. Signal Process.* **42**(8), 1905–1915.
- Chen, T., Larmat, C., Blom, P., and Zeiler, C. (2023). “Seismoacoustic analysis of the large surface explosion coupling experiment using a large-N seismic array,” *Bull. Seismol. Soc. Am.* **113**(4), 1692–1701.
- Cranz, C. (1926). *Lehrbuch Der Baslistik (Textbook of Classical Literature)* (Springer, Berlin).
- Durell, C. V. (1923). *Modern Geometry; The Straight Line and Circle* (Macmillan, London).
- Dowell, D. C., Alexander, C. R., James, E. P., Weygandt, S. S., Benjamin, S. G., Manikin, G. S., Blake, B. T., Brown, J. M., Olson, J. B., Hu, M., Smirnova, T. G., Ladwig, T., Kenyon, J. S., Ahmadov, R., Turner, D. D., Duda, J. D., and Alcott, T. I. (2022). “The High-Resolution Rapid Refresh (HRRR): An hourly updating convection-allowing forecast model. Part I: Motivation and system description,” *Weather Forecast.* **37**(8), 1371–1395.
- Eaton, S. W., Cárdenas, E. S., Hix, J. D., Johnson, J. T., Watson, S. M., Chichester, D. L., Garcés, M. A., Magaña-Zook, S. A., Maceira M., Marcillo, O. E., Chai, C., d’Entremont, B. P., and Reichardt, T. A. (2022). “An algorithmic approach to predicting mechanical draft cooling tower fan speeds from infrasound signals,” *Appl. Acoust.* **199**, 109015.
- Evans, L. B., Bass, H. E., and Sutherland, L. C. (1972). “Atmospheric absorption of sound: Theoretical predictions,” *J. Acoust. Soc. Am.* **51**(5B), 1565–1575.
- Fee, D., Toney, L., Kim, K., Sanderson, R., Iezzi, A. M., Matoza, R. S., DeAngelis, S., Jolly, A., Lyons, J. J., and Haney, M. M. (2021). “Local explosion detection and infrasound localization by reverse time migration using 3-D finite-difference wave propagation,” *Front. Earth Sci.* **9**, 620813.
- Ford, R. D., Saunders, D. J., and Kerry, G. (1993). “The acoustic pressure waveform from small unconfined charges of plastic explosive,” *J. Acoust. Soc. Am.* **94**(1), 408–417.
- Foy, W. (1976). “Position-location solutions by Taylor-series estimation,” *IEEE Trans. Aerosp. Electron. Syst.* **AES-12**(2), 187–194.
- Fuchs, F., Schneider, F. M., Kolínský, P., Serafin, S., and Bokelmann, G. (2019). “Rich observations of local and regional infrasound phases made by the AlpArray seismic network after refinery explosion,” *Sci. Rep.* **9**(1), 13027.
- Ganti, R. K., Ye, F., and Lei, H. (2011). “Mobile crowdsensing: Current state and future challenges,” *IEEE Commun. Mag.* **49**, 32–39.
- Garcés, M. A. (2019). *Explosion Source Models* (Springer International Publishing, Cham, Switzerland), pp. 273–345.
- Garcés, M. A. (2020). “Quantized constant-Q Gabor atoms for sparse binary representations of cyber-physical signatures,” *Entropy* **22**(9), 936.
- Garcés, M. A. (2023). “Quantized information in spectral cyberspace,” *Entropy* **25**(3), 419.
- Garcés, M. A., Bowman, D., Zeiler, C., Christe, A., Yoshiyama, T., Williams, B., Colet, M., Takazawa, S., and Popenhagen, S. (2022). “Skyfall: Signal fusion from a smartphone falling from the stratosphere,” *Signals* **3**(2), 209–234.
- Gitterman, Y. (2010). “Sayarim infrasound calibration explosion: Near-source and local observations and yield estimation,” in *Proceedings of the 2010 Monitoring Research Review: Ground-Based Nuclear Explosion Monitoring Technologies*, LA-UR-10-05578, 2, pp. 708–719.
- Goldstein, P., Dodge, D., Firpo, M., and Minner, L. (2003). “SAC2000: Signal processing and analysis tools for seismologists and engineers,” in *The IASPEI International Handbook of Earthquake and Engineering Seismology*, edited by W. H. K. Lee, H. Kanamori, P. C. Jennings, and C. Kisslinger (Academic, London).
- Goldstein, P., and Snoko, A. (2005). “SAC availability for the IRIS community,” Incorporated Research Institutions for Seismology Newsletter.
- Hopkinson, B. (1915). “British ordnance board minutes,” Report No. 13565, British Ordnance Office, London.
- Kim, K., and Pasyanos, M. E. (2023). “Seismoacoustic explosion yield and depth estimation: Insights from the large surface explosion coupling experiment,” *Bull. Seismol. Soc. Am.* **113**, 1457–1470.
- Kim, K., Rodgers, A. R., Garcés, M. A., and Myers, S. C. (2021). “Empirical acoustic source model for chemical explosions in air,” *Bull. Seismol. Soc. Am.* **111**(5), 2862–2880.
- Kim, K., and Rodgers, A. (2016). “Waveform inversion of acoustic waves for explosion yield estimation,” *Geophys. Res. Lett.* **43**, 6883–6890, <https://doi.org/10.1002/2016GL069624>.
- Kinney, G., and Graham, K. (1985). *Explosive Shocks in Air* (Springer-Verlag, Berlin).
- Klapötke, T. M. (2022). *Chemistry of High-Energy Materials*, 6th ed. (De Gruyter, Berlin).
- Kong, Q., Allen, R. M., and Schreier, L. (2016). “MyShake: Initial observations from a global smartphone seismic network,” *Geophys. Res. Lett.* **43**, 9588–9594, <https://doi.org/10.1002/2016GL070955>.
- Koper, K., Wallace, T. C., Reinke, R. E., and Leverette, J. A. (2002). “Empirical scaling laws for truck bomb explosions based on seismic and acoustic data,” *Bull. Seismol. Soc. Am.* **92**(2), 527–542.
- Kulichkov, S. N. (1998). “Acoustic sounding of inhomogeneous structures in the middle atmosphere,” *Izv. Atmos. Oceanic Phys.* **34**(1), 1–6.
- Kulichkov, S. N., and Bush, G. A. (2001). “Rapid variations in infrasonic signals at long distance from one-type explosions,” *Izv. Atmos. Oceanic Phys.* **37**(3), 306–313.
- Lane, N. D., Miluzzo, E., Lu, H., Peebles, D., Choudhury, T., and Campbell, A. T. (2010). “A survey of mobile phone sensing,” *IEEE Commun. Mag.* **48**, 140–150.
- Mahapatra, C., and Mohanty, A. R. (2022a). “Explosive sound source localization in indoor and outdoor environments using modified Levenberg Marquardt algorithm,” *Meas. J. Int. Meas. Confed.* **187**, 110362.
- Mahapatra, C., and Mohanty, A. R. (2022b). “Optimization of number of microphones and microphone spacing using time delay based multilateration approach for explosive sound source localization,” *Appl. Acoust.* **198**, 108998.
- Modrak, R. T., Arrowsmith, S. J., and Anderson, D. N. (2010). “A Bayesian framework for infrasound location,” *Geophysical J. Int.* **181**, 399–405.
- Pasyanos, M. E., and Kim, K. (2019). “Seismoacoustic analysis of chemical explosions at the Nevada National Security Site,” *JGR Solid Earth* **124**(1), 908–924.
- Popenhagen, S. K., Bowman, D. C., Zeiler, C., and Garcés, M. A. (2023). “Acoustic waves from a distant explosion recorded on a continuously ascending balloon in the middle stratosphere,” *Geophys. Res. Lett.* **50**(20), e2023GL104031, <https://doi.org/10.1029/2023GL104031>.
- Rosoff, H., and Von Winterfeldt, D. (2007). “A risk and economic analysis of dirty bomb attacks on the ports of Los Angeles and Long Beach,” *Risk Anal.* **27**, 533–546.
- Sachs, R. G. (1944). “The dependence of blast on ambient pressure and temperature,” technical report, DTIC Document.

- Schnurr, J., Kim, K., Garcés, M. A., and Rodgers, A. (2020). "Improved parametric models for explosion pressure signals derived from large datasets," *Seismol. Res. Lett.* **91**(3), 1752–1762.
- Silber, E. A., Bowman, D. C., and Ronac Giannone, M. (2023). "Detection of the large surface explosion coupling experiment by a sparse network of balloon-borne infrasound sensors," *Remote Sens.* **15**(2), 542.
- Slad, G., and Merchant, B. (2021). "Evaluation of low-cost infrasound sensor packages," Sandia National Laboratory.
- Stockwell, R. G., Mansinha, L., and Lowe, R. P. (1996). "Localization of the complex spectrum: The S transform," *IEEE Trans. Signal Process.* **44**(4), 998–1001.
- Sundar, H., Sreenivas, T. V., and Seelamantula, C. S. (2018). "TDOA-based multiple acoustic source localization without association ambiguity," *IEEE/ACM Trans. Audio, Speech, Lang. Process.* **26**, 1976–1990.
- Takazawa, S. K., Kim, K., and Garcés, M. A. (2023a). "Chemical Blast Standard (1 kg)," *Seismol. Res. Lett.* **94**(5), 2514–2524.
- Takazawa, S. K., Kim, K., and Garcés, M. A. (2023b). Replication Data for: Chemical Blast Standard (1 kg), Harvard Dataverse.
- Takazawa, S. K., Popenhagen, S. K., Ocampo Giraldo, L. A., Cardenas, E. S., Hix, J. D., Thompson, S. J., Chichester, D. L., and Garcés, M. A. (2024). "Replication data for: A comparison of smartphone and infrasound microphone data from a fuel air explosive and a high explosive, Harvard dataverse."
- Thandu, S. C., Chellappan, S., and Yin, Z. (2015). "Ranging explosion events using smartphones," in *2015 IEEE 11th International Conference on Wireless and Mobile Computing, Networking and Communications (WiMob)*, pp. 492–499.
- The pandas development team (2024). pandas-dev/pandas: Pandas (v2.2.2). Zenodo. <https://doi.org/10.5281/zenodo.10957263> (Last viewed August 22, 2024).
- Tsybulenko, E. (2022). "Fuel air explosive weapons," in *International Conflict and Security Law*, edited by S. Sayapin, R. Atadjanov, U. Kadam, G. Kemp, N. Zambrana-Tévar, and N. Quénivet (T.M.C. Asser, The Hague).
- Tyagi, V. B., Lokesh, S. S., Tesfaye, A., Kassa, Y., and Ababe, T. (2014). "A review paper on infrasound event detection & localization," *Int. J. Adv. Res. Electron. Commun. Eng.* **3**, 621–624.
- Vergoz, J., Hupe, P., Listowski, C., Le Pichon, A., Garcés, M. A., Marchetti, E., Labazuy, P., Ceranna, L., Pilger, C., Gaebler, P., Näsholm, S. P., Brissaud, Q., Poli, P., Shapiro, N., De Negri, R., and Mialle, P. (2022). "IMS observations of infrasound and acoustic-gravity waves produced by the January 2022 volcanic eruption of Hunga, Tonga: A global analysis," *Earth Planet. Sci. Lett.* **591**, 117639.
- Welch, P. (1967). "The use of fast Fourier transform for the estimation of power spectra: A method based on time averaging over short, modified periodograms," *IEEE Trans. Audio Electroacoust.* **15**(2), 70–73.
- Wildegger-Gaissmaier, A. E. (2004). "Aspects of thermobaric weaponry," *Mil. Technol.* **28**(6), 125–126.
- Young, E. F., Bowman, D. C., Lees, J. M., Klein, V., Arrowsmith, S. J., and Ballard, C. (2018). "Explosion-generated infrasound recorded on ground and airborne microbarometers at regional distances," *Seismol. Res. Lett.* **89**(4), 1497–1506.